IEEE Access
Multidisciplinary | Rapid Review | Open Access Journal

Received November 25, 2019, accepted December 27, 2019, date of publication January 13, 2020, date of current version January 22, 2020.

Digital Object Identifier 10.1109/ACCESS.2020.2965973

A Bayesian Angular Superresolution Method With Lognormal Constraint for Sea-Surface Target

JIANYU YANG, (Member, IEEE), YAO KANG, YIN ZHANG, (Member, IEEE), YULIN HUANG, (Senior Member, IEEE), AND YONGCHAO ZHANG, (Member, IEEE)
School of Information and Communication Engineering, University of Electronic Science and Technology of China, Chengdu 611731, China

Corresponding authors: Yao Kang (yaoyao_kang@163.com) and Yin Zhang (yinzhang@uestc.edu.cn)

This work was supported by the National Natural Science Foundation of China under Grant 61671117 and 61901090.

ABSTRACT Maximum a posteriori (MAP) approach, based on Bayesian criterion, is proposed to overcome the low azimuth resolution in real-aperture imaging. The essence of this approach is to use the statistical characteristics of the imaging background and target to invert the real target scene. This paper presents a deconvolution method based on Maximum a posteriori (MAP) criterion, which combines the Rayleigh distribution and Lognormal distribution, to realize high angular resolution for sea-surface target. Firstly, Rayleigh distribution is considered to express the statistical properties of sea clutter. Moreover, the Lognormal distribution is employed to represent the statistical properties of target as prior information. The reason is that Lognormal distribution can be approximatively regarded as a combined constraint term. Finally, the optimization theory is utilized to obtain the iterative estimated solution. The processed results of simulation and measured data are given to verify the performance of proposed algorithm.

INDEX TERMS Radar imaging, angular superresolution, lognormal restrict, sea-surface target.

I. INTRODUCTION

The reconnaissance and detection of sea-surface target are of crucial importance, which are applied to marine environmental monitoring, marine vessel detection and maritime rescue. In particular, it plays an indispensable role in the situational awareness of the sea battlefield. Real-aperture scanning radar imaging is a significant technology to achieve the reconnaissance and detection of sea-surface target because it is suitable for most geometry situation [1]. However, the angular resolution of this radar system is greatly limited by the antenna aperture size, which seriously influences the searching ability and location accuracy [2], [3]. Over the years, the proposed angular superresolution approaches are applied to the ground scenarios mostly. Therefore, it is urgent for us to propose effective methods to improve the angular resolution of real-aperture radar for sea-surface target.

So far, the angular superresolution methods can be divided into three categories. One is the traditional spectral estimation method [4]–[6], represented by multiple signal classification (MUSIC) method. However, how to collect enough snapshots to realize the high estimation precision of the covariance matrix is difficult for the mechanical scanning radar system [7], [8]. In recent years, an iterative adaptive approach (IAA) was presented, which can significantly decrease the requirement of snapshots in traditional method. Some effects have been gained by applying this approach to the real-aperture angular superresolution problem [9], [10]. Besides, there are two main categories of deconvolution techniques based on regularization theory and Bayes criterion, respectively. The core of regularization theory is to model the unknowns as a deterministic function, where the errors are Gaussian noise. The pseudo-inverse solution is regarded as an optimal solution. In the references [11], [12], the authors proposed a truncated singular value decomposition (TSVD) method with the intention of suppressing noise amplification. It is able to reduce the influence of noise in the solving process and suitble for low noise environment. Another class of methods with additional regular terms to balance the effect of noise suppression and target prior, such as $l_1 - norm$ and

The associate editor coordinating the review of this manuscript and approving it for publication was Ravibabu Mulaveesala.

$l_2 - norm$, are widely studied by researchers [13], [14]. However, the constraint of single regular term only can be applied to the specific imaging scene, so the adaptability on different scenes is poor.

The traditional spectral estimation method and regularization method are mainly applied to ground target. It is deemed that the noise satisfies the Gaussian distribution, and the sea clutter characteristics are not considered. Therefore, the imaging performance of the above two methods is poor when they are applied to the sea target.

Bayesian deconvolution approaches, relying on the statistical characteristics of noise and the prior knowledge of target scatters, can convert the solving problem of angular superresolution into maximum a posterior probability (MAP) estimation [15], [16]. In these references [17]–[19], the MAP method was presented based on the assumption that the statistic of noise obeys Gaussian or Poisson distribution, which is effective in the process of recovering land target. However, the imaging results of these methods above are undesired facing the problem of sea-surface environment.

The essence of angular superresolution imaging on sea-surface target is to improve angular resolution under the condition of suppressing sea clutter. Sea clutter is complicated and changeable under the interference of natural climate, and the previous assumptions are no longer suitable for sea-surface environment. Therefore, the sea-surface background and the target prior need to be modeled again in the sea-surface environment. Bayesian approach need to choose the reasonable likelihood function and prior information.

The likelihood function is mainly used to represent the distribution characteristics of clutter, which can effectively reduce the estimation error in the solving process of algorithm. The existing methods in [20], [21] usually consider that the clutter in the received echo obeys Gaussian or Poisson distribution, and they can be applied to the ground-target imaging well. However, these distribution characteristics can not truly reflect the sea surface background dominated by sea clutter. Researches show that the distribution of sea clutter approximately obeys K distribution [22], Rayleigh distribution [23] and Log-normal distribution [24]. In reference [25], the authors presented a maximum likelihood (ML) approach, whose likelihood function is Rayleigh distribution. The simulation results show the effective improvement of azimuth resolution under the background of sea clutter, but the property of clutter suppression and imaging quality is insufficient due to the lack of prior information.

Prior information expressed as probability density function represents the statistical characteristics of target backscatter coefficient, which is employed for high angular resolution and image quality [26]. The sparse distribution is usually considered as the prior information in real aperture imaging because in most cases, the distribution of strong scattering target is sparse relative to the imaging area [27]. It can greatly improve the azimuth resolution of target imaging, but the drawbacks of this constraint are losing imaging quality and the false target will appear when the signal to noise ratio (SNR) is low. In addition, the smoothing property of Gaussian distribution is in favor of the enhancement of imaging quality, but the improvement in azimuth resolution is limited [28], [29].

In this paper, a novel MAP method is proposed by combining Rayleigh-based ML approach and Lognormal distribution as prior information. It has been verified in [30]and [31] that the major statistical models of K distribution and Weibull distribution that have been proposed for the statistics of sea clutter may be represented as a Rayleigh mixture model. Therefore, Rayleigh distribution is well suited for describing the statistic property of sea clutter. And the Lognormal distribution [32]–[34], as a heavy-tailed distribution which means the probability of strong scatters is large, can catch the strong targets easily. In addition, the Lognormal distribution can be approximatively regarded as a combined constraint term, and it possesses better smooth features compared with the common sparse distribution.

This paper is organized as follows. The imaging model of the real aperture scanning radar is described in Section II. In Section III, the MAP method based on the hypothesis that the sea clutter and targets obey the Rayleigh distribution and Log-normal distribution is derived in detail. Section IV shows the processed results of simulation and measured data as well as the analysis of the handled image. Conclusions are discussed in Section V.

II. IMAGING MODEL OF REAL APERTURE SCANNING RADAR

In this section, we mainly describe the angular superresolution model which emphasis on the echo formulation. Figure 1 shows the geometric model of the real aperture scanning radar. In the scanning imaging model, the airborne platform moves on with a uniform velocity V, and the radar antenna counterclockwise sweeps across forward-looking imaging region containing targets $l_1 \sim l_k$. H and ω repre-

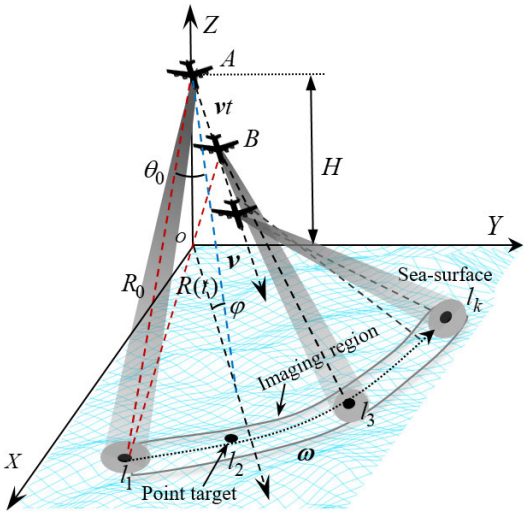

FIGURE 1. Geometric model of the real aperture scanning radar.

sent the flight height of airborne platform and the scanning speed of the antenna, respectively. R_0 is initial range history between the antenna and l_1. After a time interval t, the range history $R(t)$ can be expressed as

$$R(t) = \sqrt{R_0^2 + V^2t^2 - 2R_0Vt\cos\theta_0}, \tag{1}$$

where θ_0 is forward-looking angle. Simplify Eq.(1) by Taylor expansion and $R(t)$ can be written as

$$R(t) \approx R_0 - Vt\cos\theta_0 + \frac{V^2\sin\theta_0^2}{2R_0}t^2. \tag{2}$$

In practical applications, the time to sweep through a target is very short. In addition, forward-looking scanning radar generally has a long range history. Thus, the influence of the quadratic term on the range history is often ignored and Eq.(2) can be further simplified as

$$R(t) \approx R_0 - Vt\cos\theta_0. \tag{3}$$

The antenna transmits linear frequency modulation (LFM) signal to achieve high range resolution. The specific formulae of the LFM signal is

$$g(\tau) = rect\left[\frac{\tau}{T_r}\right]\exp\left(j2\pi f_0\tau + j\pi K_r\tau^2\right), \tag{4}$$

where τ denotes the fast time, and T_r is the pause width of the LFM. f_0 and K_r mean the carrier frequency and frequency modulation slope, separately. The window function can be expressed as

$$rect\left[\frac{\tau}{T_r}\right] = \begin{cases} 1, & \tau < \frac{T_r}{2} \\ 0, & others \end{cases}. \tag{5}$$

After the antenna scans whole forward-looking imaging region, the discrete two-dimensional echo signal processed by the down-conversion can be expressed as

$$g(t,\tau) = \sum_{j=1}^{M}\sum_{i=1}^{N}\sigma_{ij}A(t)rect\left(\frac{\tau-\tau_d}{T_r}\right)\exp\left[j\pi K_r(\tau-\tau_d)^2\right] \times \exp\left(-j2\pi f_0\tau_d\right), \tag{6}$$

where $g(t,\tau)$ denotes the echo signal and t is the slow time. M and N represent the sampling number in range and azimuth, respectively. σ_{ij} means the scatting amplitude of target located at ith azimuth and jth range bin and $A(t)$ is the antenna pattern modulation. τ_d=$2R(t)/c$ represents the time delay and c is the velocity of light.

Pulse compression and range walk correction can realize high range resolution. After these processes, the echo signal can be transformed as

$$g(t,\tau) = \sum_{j=1}^{M}\sum_{i=1}^{N}\sigma_{ij}A(t)\sin c\left\{B\left[\tau - \frac{2R_0}{c}\right]\right\} \times \exp\left\{-j\pi f_0\frac{4R(t)}{c}\right\}. \tag{7}$$

According to $t = (\theta - \theta_0)/\omega$, Eq.(7) can be written as

$$g(R,\theta) = \sum_{j=1}^{M}\sum_{i=1}^{N}\sigma_{ij}A(\theta-\theta_0)\sin c\left\{\frac{2B}{c}[R-R_0]\right\} \times \exp\left\{-j\frac{4\pi}{\lambda}V\frac{\theta-\theta_0}{\omega}\cos\theta_0\right\}. \tag{8}$$

$\exp\left\{-j\frac{4\pi}{\lambda}V\frac{\theta-\theta_0}{\omega}\cos\theta_0\right\}$ is the Doppler shift, which can usually be ignored in practice. In other words, the Doppler shift is zero for static platform and has small effect to the echo signal for the motion plat form with low speed moving or high speed scanning [13]. The received echo can be written as the following two-dimensional convolution model

$$\boldsymbol{g}(R,\theta) = \boldsymbol{H}(R,\theta)\otimes\boldsymbol{f}(R,\theta), \tag{9}$$

where $\boldsymbol{g}(R,\theta)$ is the received two-dimensional signal, R and θ represent the range and azimuth variable of the two-dimensional signal, respectively. $\boldsymbol{H}(R,\theta)$ is the two-dimensional convolution kernel function and $\boldsymbol{f}(R,\theta)$ is the target scattering distribution. The high resolution can be easily achieved by transmitting a large bandwidth LFM signal in range dimension, and the range resolution is decided by the 3-dB width of the convolution kernel *sinc* function, which can be calculated by $c/2B$. In azimuth dimension, the kernel function is the antenna pattern, and the azimuth resolution is limited by the size of real aperture which leads to the unmatched two-dimensional resolution. This paper presents a new deconvolution method for high azimuth resolution. We first rearrange Eq.(9) as the following matrix form

$$\begin{aligned}\boldsymbol{g} &= \boldsymbol{H}\boldsymbol{f} + \boldsymbol{n} \\ &= \begin{bmatrix} H_{N\times K} & & \\ & \ddots & \\ & & H_{N\times K}\end{bmatrix}\begin{bmatrix} f(1,1) \\ f(1,2) \\ \vdots \\ f(1,K) \\ \vdots \\ f(M,K)\end{bmatrix} + \boldsymbol{n},\end{aligned} \tag{10}$$

$$H_{N\times K} = \begin{bmatrix} h_1 & 0 & 0 & 0 & \\ h_2 & h_1 & \vdots & \vdots & \\ \vdots & h_2 & \ddots & h_1 & 0 \\ h_L & \vdots & \ddots & h_2 & h_1 \\ 0 & h_L & \ddots & \vdots & h_2 \\ \vdots & \vdots & h_L & \vdots & \\ 0 & 0 & 0 & h_L & \end{bmatrix}, \tag{11}$$

where $\boldsymbol{g} = [g(1,1), g(1,2), \cdots, g(1,N), \cdots, g(M,N)]^T$ represents the two-dimensional echo measurements which is rearranged in azimuth dimension with size $MN\times 1$, and M, N are the sampling numbers of the received echo in range and azimuth dimension, respectively.

$\boldsymbol{f} = [f(1,1), f(1,2), \cdots, f(1,K), \cdots, f(M,K)]^T$ denotes the unknown imaging scene amplitude values which

is rearranged in azimuth dimension with size $MK \times 1$, and K is the discrete number in azimuth of imaging scene. n represents the additive clutter and noise vector with size $MN \times 1$. Matrix H is the convolution measurement matrix with size $MN \times MK$. This matrix is composed of $H_{N\times K}$ which is the convolution measurement matrix of the single range unit, and $H_{N\times K}$ can be written as Eq.(10).

Where the elements of Eq.(11) are the weighed value of the antenna pattern to the corresponding target at different sampling times, and L denotes the discrete number of antenna pattern. The goal of radar imaging with high azimuth resolution is to accurately infer $\boldsymbol{f}$ from the echo signal $\boldsymbol{g}$. Based on the convolution model of $\boldsymbol{g}$ and $\boldsymbol{f}$, this task is called deconvolution problem in this paper. However, direct division in the frequency domain is unstable and impracticable for radar system due to the band-limited character of antenna pattern in the frequency domain and the influence of echo noise, which is called ill-posed nature for direct deconvolution [35], [36].

Eq.(11) can be regarded as the classical signal recovery problem in estimation theory. In the next section, a MAP deconvolution algorithm is proposed based on the property of the sea clutter and target.

III. BAYESIAN SUPERRESOLUTION METHOD

In this section, we convert the deconvolution problem into an equivalent maximum a posterior (MAP) estimation task. The MAP algorithm is a typical superresolution approach which is based on the Bayesian framework

$$p(\boldsymbol{f}\,|\boldsymbol{g}) = \frac{p(\boldsymbol{g}|\boldsymbol{f})p(\boldsymbol{f})}{p(\boldsymbol{g})}, \tag{12}$$

where $p(\boldsymbol{f}\,|\boldsymbol{g})$ is the posteriori probability, $p(\boldsymbol{g}\,|\boldsymbol{f}\,)$ is the likelihood probability and $p(\boldsymbol{f})$ is the prior knowledge of target scattering coefficient. The estimated value $\hat{\boldsymbol{f}}$ is acquired by the maximum a posterior (MAP) criterion, which satisfies

$$\begin{aligned}\widehat{\boldsymbol{f}} &= \arg\max_{\boldsymbol{f}} p(\boldsymbol{f}\,|\boldsymbol{g}) = \arg\max_{\boldsymbol{f}} p(\boldsymbol{g}\,|\boldsymbol{f}\,)p(\boldsymbol{f}) \\ &= \arg\min_{\boldsymbol{f}} \{-\ln p(\boldsymbol{g}\,|\boldsymbol{f}\,) - lnp(\boldsymbol{f})\}.\end{aligned} \tag{13}$$

In this paper, it is assumed that the noise in each observed cell obeys independent Rayleigh distribution [23] so that the likelihood function can be written as

$$p(\boldsymbol{g}|\boldsymbol{f}) = \prod_i \frac{\boldsymbol{g}_i - (\boldsymbol{H}\boldsymbol{f})_i}{\sigma^2} \exp\left\{-\frac{[\boldsymbol{g}_i - (\boldsymbol{H}\boldsymbol{f})_i]^2}{2\sigma^2}\right\}, \tag{14}$$

where i is the sampling cell, $(\boldsymbol{H}\boldsymbol{f})_i = \sum_{j=1}^{MK} h_{ij}\boldsymbol{f}_j$, $i \in 1 \sim MN$, and σ^2 indicates the parameter of Rayleigh distribution which affects the mean and variance. It has been verified in [30] and [31] that Rayleigh assumption is well suited for describing the statistic property of sea clutter. Moreover, the Rayleigh-based ML approach in [25] has demonstrated the feasibility of superresolution imaging for sea-surface target.

Prior knowledge plays an important role in Bayesian method. It is helpful to approximate the optimal solution during the iterations. The introduction of reasonable prior knowledge for the target scene could significantly improve the imaging performance. This paper introduces Lognormal distribution as the prior distribution of sea-surface target, for the reason that Lognormal distribution [37] as a heavy-tailed distribution can catch the strong targets easily, and it can be approximatively regarded as a combined constraint term. It possesses better smooth features comparing with the common sparse distribution. And the Lognormal distribution function can be written as

$$p(\boldsymbol{f}) = \prod_j \frac{1}{\boldsymbol{f}_j \eta\sqrt{2\pi}} \exp\left\{-\frac{(\ln \boldsymbol{f}_j - \mu)^2}{2\eta^2}\right\}, \tag{15}$$

where μ, η represent the distribution parameter of the Lognormal, which restrict the mean and variance. $\boldsymbol{f}_j$ is the j-th element of $\boldsymbol{f}$. Combining Eq.(14) and Eq.(15), the posteriori probability function with negative-logarithm operation becomes

$$\begin{aligned}&-\ln p(\boldsymbol{g}|\boldsymbol{f}) - lnp(\boldsymbol{f}) \\ &= \sum_i \left[-\ln[\boldsymbol{g}_i - (\boldsymbol{H}\boldsymbol{f})_i] + \ln\sigma^2 + \frac{[\boldsymbol{g}_i - (\boldsymbol{H}\boldsymbol{f})_i]^2}{2\sigma^2}\right] \\ &\quad + C\ln(2\pi\eta^2) + \sum_j \ln(\boldsymbol{f}_j) + \frac{1}{2\eta^2}\sum_j (\ln \boldsymbol{f}_j - \mu)^2,\end{aligned} \tag{16}$$

where C is a constant.

In order to obtain the optimization solution of the estimated value $\hat{\boldsymbol{f}}$ acquired by the maximum a posterior (MAP) criterion, we let $\boldsymbol{T} = -\ln p(\boldsymbol{g}|\boldsymbol{f}) - lnp(\boldsymbol{f})$, and calculate the gradient of Eq.(16) with respect to $\boldsymbol{f}$

$$\begin{aligned}\nabla_f(\boldsymbol{T}) = \boldsymbol{H}^T \frac{1}{\boldsymbol{g} - \boldsymbol{H}\boldsymbol{f}} - \frac{1}{\sigma^2}\boldsymbol{H}^T(\boldsymbol{g} - \boldsymbol{H}\boldsymbol{f}) \\ + \frac{1}{\mathbf{f}} + \frac{1}{\eta^2} \times \frac{1}{\mathbf{f}} \times \ln \mathbf{f} - \frac{\mu}{\eta^2} \times \frac{1}{\mathbf{f}},\end{aligned} \tag{17}$$

where the $\times$ represents dot product of vectors. For simple expression, Eq.(17) is rewritten as the following form

$$\nabla_f(\boldsymbol{T}) = \boldsymbol{H}^T \frac{1}{\boldsymbol{g} - \boldsymbol{H}\boldsymbol{f}} - \frac{1}{\sigma^2}\boldsymbol{H}^T(\boldsymbol{g} - \boldsymbol{H}\boldsymbol{f}) + \boldsymbol{P}\boldsymbol{f}, \tag{18}$$

where matrix $\mathbf{P} = diag\{\cdots, p_i, \cdots\}, p_i = \frac{1}{\mathbf{f}_i^2} + \frac{1}{\eta^2} \times \ln(\mathbf{f}_i) \times \frac{1}{\mathbf{f}_i^2} - \frac{\mu}{\eta^2} \times \frac{1}{\mathbf{f}_i^2}$. Then we can minimize Eq.(18) by letting $\nabla_f(\boldsymbol{T}) = 0$, and simple solution is derived as

$$\boldsymbol{f} = (\frac{1}{\sigma^2}\boldsymbol{H}^T\boldsymbol{H} + \boldsymbol{P})^{-1}(\frac{1}{\sigma^2}\boldsymbol{H}^T\boldsymbol{g} - \boldsymbol{H}^T\frac{1}{\boldsymbol{g} - \boldsymbol{H}\boldsymbol{f}}). \tag{19}$$

We can obtain the iterative expression from Eq.(19)

$$\boldsymbol{f}^{(k+1)} = (\frac{1}{\sigma^2}\boldsymbol{H}^T\boldsymbol{H} + \boldsymbol{P}^{(k)})^{-1}(\frac{1}{\sigma^2}\boldsymbol{H}^T\boldsymbol{g} - \boldsymbol{H}^T\frac{1}{\boldsymbol{g} - \boldsymbol{H}\boldsymbol{f}^{(k)}}), \tag{20}$$

where k represents the iteration index, $\boldsymbol{P}^{(k)}$ is calculated by $\boldsymbol{f}^{(k)}$, and the initial value of iteration $\boldsymbol{f}^{(1)}$ is simply represented by the received data $\boldsymbol{g}$.

In addition, the estimation method based on the maximum likelihood(ML) is used to estimate the statistical parameters of the Rayleigh distribution. The sea clutter signal is sampled as sequence $c_1, c_2 \cdots c_L$, where $c_i = \boldsymbol{g}_i - (\boldsymbol{Hf})_i$ and L is sampling points. The log-likelihood function of Rayleigh distribution can be transformed as

$$L_{ML}(\boldsymbol{c}, \sigma) = -L \ln \sigma^2 + \sum_{i=1}^{L} \ln c_i - \sum_{i=1}^{L} \frac{(c_i)^2}{2\sigma^2}. \quad (21)$$

The parameter estimate of σ is obtained by setting the gradient of Eq.(21) to zero.

$$\frac{\partial L_{ML}(\boldsymbol{c}, \sigma)}{\partial \sigma} = -\frac{2L}{\sigma} + \frac{1}{\sigma^3} \sum_{i=1}^{L} (c_i)^2 = 0. \quad (22)$$

Solving the above Eq.(22), we can obtain the expression of σ based on ML estimation as

$$\sigma^2 = \frac{\sum_{i=1}^{L} (c_i)^2}{2L} \quad (23)$$

The performance of the proposed MAP algorithm also relies on the parameters μ and η from the prior function.

The smaller the η is, the closer is the estimate to the smooth imaging, and the larger the η is, the less the result is influenced by the prior [26]. In practice, we need to select suitable parameters to balance clutter amplification and angular superresolution. The proposed MAP algorithm was listed in TABLE 1, where K is the iterations.

TABLE 1. Flow chart of the proposed MAP algorithm.

Initialize: μ ,η

for k=1

$$\boldsymbol{f}^{(1)} = \boldsymbol{g}, (\sigma^{(k)})^2 = \frac{\sum_{i=1}^{L} \left(\boldsymbol{g}_i - (\boldsymbol{Hf})_i\right)^2}{2L}$$

$$\boldsymbol{P}^{(k)} = diag\left\{\cdots, {p_i}^{(k)}, \cdots\right\},$$

$${p_i}^{(k)} = \frac{1}{\left(\boldsymbol{f}_i^{(k)}\right)^2} + \frac{1}{\eta^2} \times \ln(\boldsymbol{f}_i^{(k)}) \times \frac{1}{\left(\boldsymbol{f}_i^{(k)}\right)^2} - \frac{\mu}{\eta^2} \times \frac{1}{\left(\boldsymbol{f}_i^{(k)}\right)^2}$$

end

for k=2:K

$$\boldsymbol{f}^{(k)} = \left(\frac{1}{(\sigma^{(k-1)})^2} \boldsymbol{H}^T \boldsymbol{H} + \boldsymbol{P}^{(k-1)}\right)^{-1} \cdot \left(\frac{1}{(\sigma^{(k-1)})^2} \boldsymbol{H}^T \boldsymbol{g} - \boldsymbol{H}^T \frac{1}{\boldsymbol{g} - \boldsymbol{H}\boldsymbol{f}^{(k-1)}}\right)$$

$$\boldsymbol{P}^{(k)} = diag\left\{\cdots, {p_i}^{(k)}, \cdots\right\},$$

$${p_i}^{(k)} = \frac{1}{\left(\boldsymbol{f}_i^{(k)}\right)^2} + \frac{1}{\eta^2} \times \ln(\boldsymbol{f}_i^{(k)}) \times \frac{1}{\left(\boldsymbol{f}_i^{(k)}\right)^2} - \frac{\mu}{\eta^2} \times \frac{1}{\left(\boldsymbol{f}_i^{(k)}\right)^2}$$

$$(\sigma^{(k)})^2 = \frac{\sum_{i=1}^{L} \left(\boldsymbol{g}_i - (\boldsymbol{Hf})_i\right)^2}{2L}$$

end

IV. SIMULATON RESULTS

In this section, the simulation results and the analysis of the handled image are given to verify the performance of proposed RLGMAP algorithm. The point target simulation is performed by different algorithms at $SCR = 20$ and $SCR = 10$ respectively, and resolution performance of the proposed algorithm and other traditional algorithms are compared. Besides, the iterative error curves are compared with different superresolution algorithms to verify the convergence property. At last, the real data was further processed to validate the performance of proposed algorithm in practice.

A. SIMULATION RESULTS OF POINT TARGETS

In this subsection, the simulation results are two parts that they are point target and iterative error curve in different signal to clutter ratio (*SCR*). In the first part, the point target simulations by ten times' Monte Carlo experiments are processed under different algorithms, which include the TSVD algorithm, Rayleigh-based ML algorithm, IAA algorithm, Guassian-based sparse MAP (GSMAP) algorithm and proposed algorithm(RLGMAP). In the second part, iterative error curve simulation results of different algorithms are presented. The angular Superresolution and stability of the RLGMAP are verified. The detailed simulation parameters are given in Table 2.

TABLE 2. Simulation parameters.

Parameter	Value	Units
Carrier frequency	9.6	GHz
Band width	20	MHz
Antenna scanning velocity	30	$^\circ/s$
Main-lobe beamwidth	3	$^\circ$
Antenna scanning area	$-6 \sim +6$	$^\circ$
Pulse repetition frequency	1000	Hz

Because the noise is invertable in practice, the Rayleigh noise is added into the echo signal.

$$SCR = 10log_{10} \frac{\|\boldsymbol{f}\|_2}{\|\boldsymbol{g} - \boldsymbol{Hf}\|_2}, \quad (24)$$

where $\|\cdot\|$ represents the 2-norm.

Three point targets are set at -2°, 1°, 1.5° with the same amplitude. The echo signal is obtained after range compression and migration correction. Fig.2(a) and Fig.3(a) are the Real-beam echo signal. Ten times' Monte Carlo experiments are also processed by the TSVD, Rayleigh-based ML, IAA, GSMAP, proposed RLGMAP algorithm at $SCR = 20dB$ and $SCR = 10dB$, respectively. The simulation results are shown from Fig.2(b) to Fig.2(f) and Fig.3(b) to Fig.3(f). In order to compare the performance of algorithms

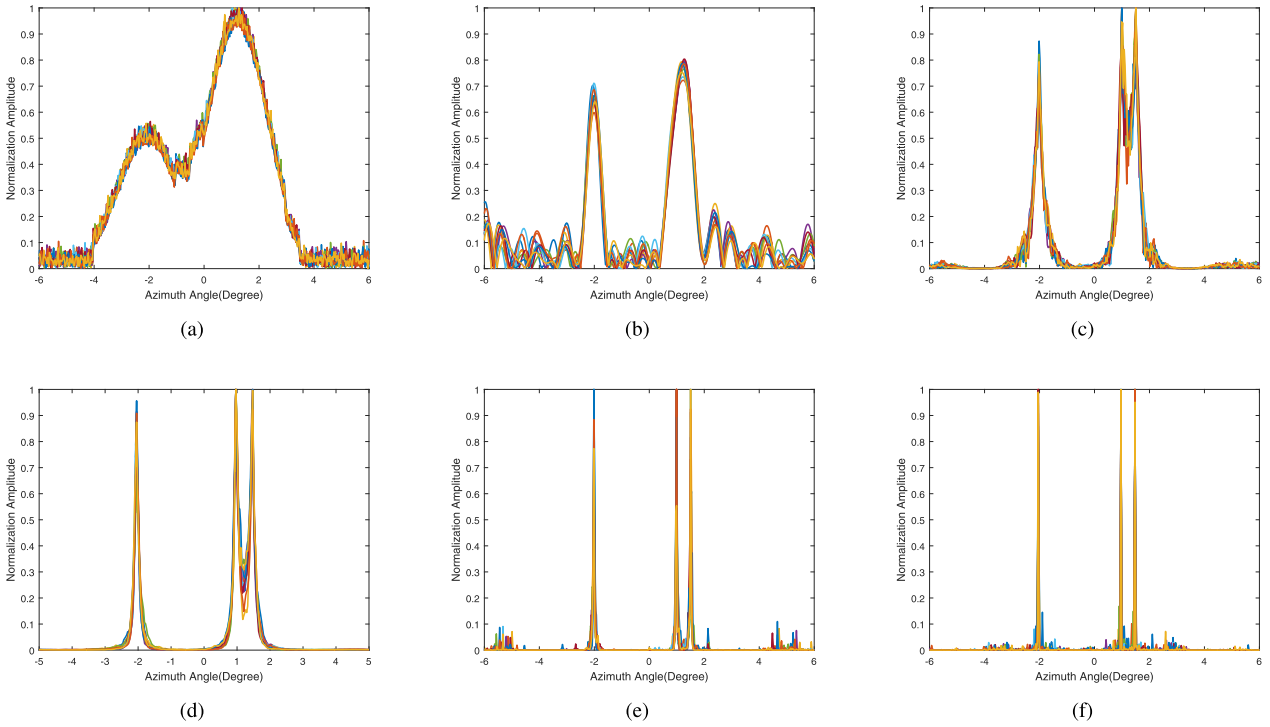

FIGURE 2. The simulation results of point target when the SCR is 20dB. (a) Real-beam echo signal, (b) TSVD algorithm, (c) Rayleigh-based ML algorithm, (d) IAA algorithm, (e) GSMAP algorithm, (f) Proposed MAP algorithm.

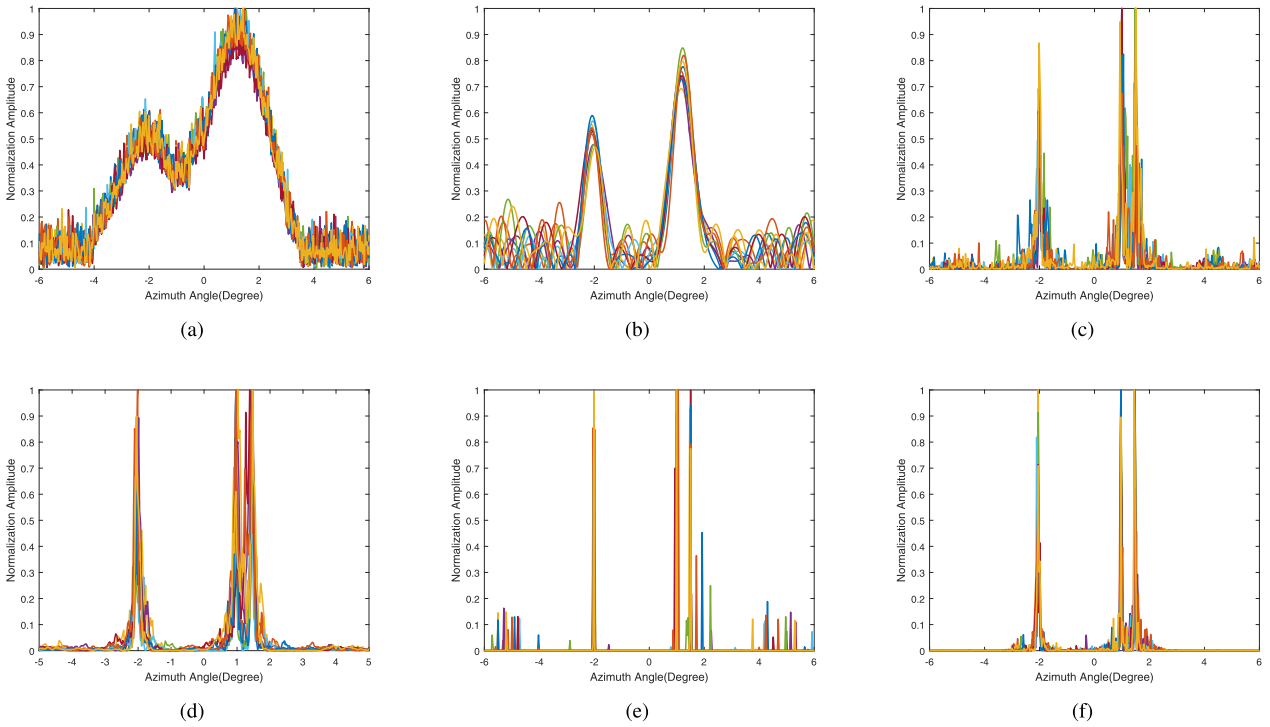

FIGURE 3. The simulation results of point target when the SCR is 10dB. (a) Real-beam echo signal, (b) TSVD algorithm, (c) Rayleigh-based ML algorithm, (d)IAA algorithm, (e) GSMAP algorithm, (f) Proposed MAP algorithm.

effectively, all simulation results are normalized amplitude. In Fig.2, it is clear that the Real-beam echo signal takes on low angular resolution. The angular resolution of TSVD is improved, but the sharpening ability is limited. The Rayleigh-based ML algorithm and IAA algorithm have a good effect on distinguishing adjacent point targets, but the saddle of

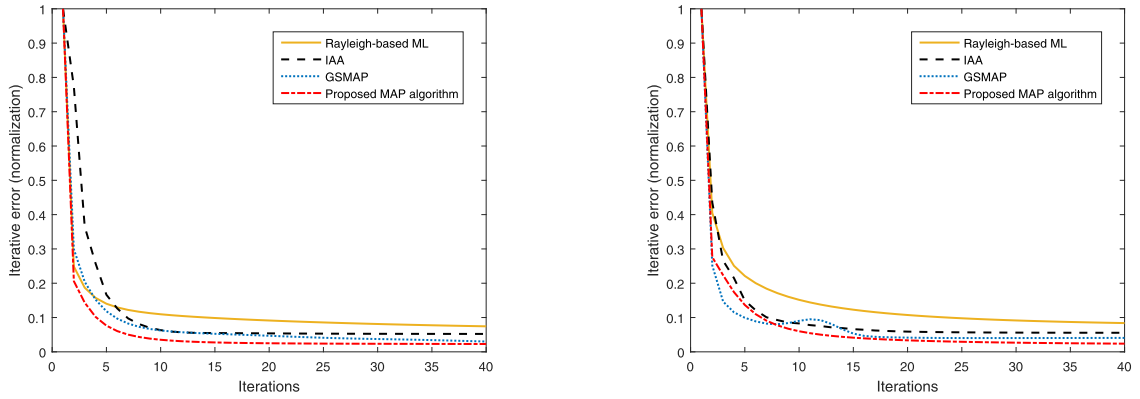

FIGURE 4. The normalized iterative error curves. (a) Rayleigh distribution when the SCR is 20 dB, (b) Rayleigh distribution when the SCR is 10 dB.

adjacent targets is high and the Rayleigh-based ML algorithm has unequal amplitudes of point targets. Compared with the IAA algorithm, the resolution performance and the ability of clutter suppression processed by the GSMAP algorithm and proposed algorithm can be greatly improved. It can be seen that the GSMAP algorithm and proposed algorithm can more effectively distinguish adjacent targets with the lower saddle than others.

The effect of clutter on imaging performance is significant in Fig.3. Processed by ten times' Monte Carlo experiments, the IAA algorithms recovers the original scene targets no better than the Rayleigh-based ML algorithm, and the adjacent targets located at 1° and 1.5° both are seriously mixed together for the two algorithms. The GSMAP algorithm can recover the original scene targets at $SCR = 20dB$, but the simulation result shows the unexpected false targets at $SCR = 10dB$. However, the proposed method can obtain better robustness of angular resolution and noise suppression ability than other methods.

We characterize the convergence property by the iteration error, which is defined as

$$e^i = \left\| \boldsymbol{g} - \boldsymbol{H}\boldsymbol{f}^i \right\|_2 \tag{25}$$

where e^i means the iteration error after i iterations and f^i is the estimation of imaging scene amplitude values after i iterations.

Fig.4(a) shows a plot of the normalized iterative error curves in Rayleigh distribution when the *SCR* is 20 dB. The Rayleigh-based ML algorithm has stable convergence performance, but the iterative error is higher than other methods. Oppositely, the convergence speed of the other algorithms is lower than Rayleigh-based ML algorithm, whereas the iterative error is low. The IAA algorithm and GSMAP both have stable convergence after 7 iterations, but the proposed RLGMAP algorithm can converge well in less than 7 iteratins with lower iteration errors, which shows that the proposed algorithm has the advantage of envergence property over other methods.

Fig.4(b) shows a plot of the normalized iterative error curves in Rayleigh distribution when the *SCR* is 10 dB. In this low *SCR* condition, the Rayleigh-based ML algorithm, IAA algorithm, GSMAP algorithm and proposed method's convergence speed slows down. The Rayleigh-based ML algorithm also has higher iterative error. In particular, the iterative error curve of the GSMAP algorithm produces a fluctuation and iteration number of convergence is greater than 15. However, the proposed RLGMAP algorithm has a good convergence speed and low normalized iterative error.

B. REAL DATA PROCESSING

Above simulation results have verified angular superresolution of the proposed RLGMAP algorithm in Rayleigh distribution. In this section, the real data was processed by the RLGMAP and other traditional algorithms to verify imaging performance in practical sea-surface targets. The original scene is shown in Fig.5 with some lands and the superresolution targets of two ships in the red circle, and the picture is from Google Earth. The real data was recorded by an X-band radar whose main system parameters were listed in TABLE 3.

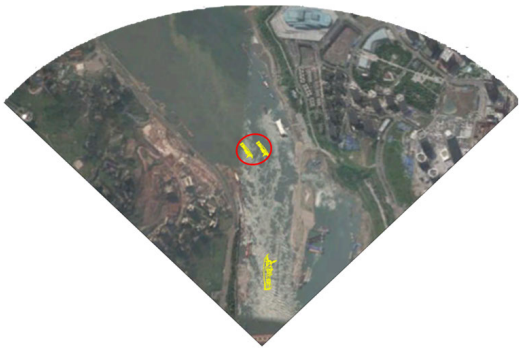

FIGURE 5. Original scene of real data.

The superresolution results of measured data processed by different algorithms are shown in Fig.6. From the Fig.6.(a),

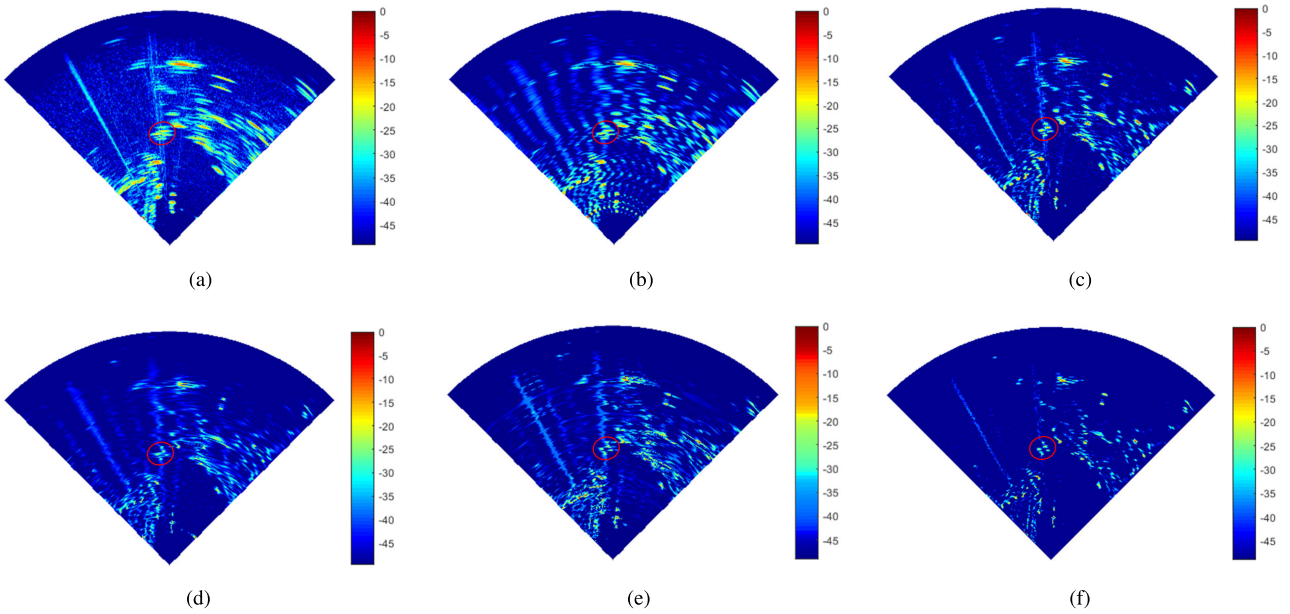

FIGURE 6. Simulation results of real data. (a) Real-beam echo signal, (b) TSVD algorithm, (c) Rayleigh-based ML algorithm, (d)IAA algorithm, (e) GSMAP algorithm, (f) Proposed MAP algorithm.

TABLE 3. Simulation parameters.

Parameter	Value	Units
Carrier frequency	9.6	GHz
Band width	75	MHz
Antenna scanning velocity	72	$^\circ/s$
Main-lobe beamwidth	5.1	$^\circ$
Antenna scanning area	$-45 \sim +45$	$^\circ$
Pulse repetition frequency	200	Hz

we can see that real beam echo has low resolution and many targets are merged by clutters. Fig.6.(b) and Fig.6.(c) show the results processed by the TSVD algorithm and Rayleigh-based ML algorithm, respectively. The TSVD algorithm has poor resolution improvement, thus adjacent ships marked in red circle are almost undistinguishable in azimuth, and the imaging result produces more obvious parasitic ripples. The Rayleigh-based ML algorithm has improved resolution performance and the ability of clutter suppression, but the sharpening ability is limited. The imaging results of the IAA algorithm and GSMAP algorithm are shown in Fig.6.(d) and Fig.6.(e), respectively. The two methods can basically distinguish adjacent ships, but they amplify the clutter, resulting in parasitic ripples that cannot be ignored. Compared with the imaging results of GSMAP algorithm, the proposed RLGMAP algorithm shown in Fig.6.(f) has greatly improved the resolution of targets estimation under sea clutter interference. That is to say, not only the adjacent ships are distinguished clearly, but also the noise level is lower than others. We can see that the proposed RLGMAP algorithm can obtain better superresolution of angular and noise suppression ability than other methods.

To further verify the superresolution performance, the profiles of two adjacent targets marked by red circle are shown in Fig.7. From the profiles,we can find that the TSVD algorithm and Rayleigh-based ML algorithm only can sharpen the real beams lightly with a high saddle. The IAA algorithms can achieve higher resolution than above two algorithms, but the resolution improvement is limited compared with the GSMAP algorithm and proposed RLGMAP algorithm. Obviously, the GSMAP algorithm and proposed RLGMAP algorithm can achieve higher resolution with lower saddle than other algorithms, but their performance was not the same. We can find that the profile of GSMAP algorithm generates the unexpected false target, and the proposed

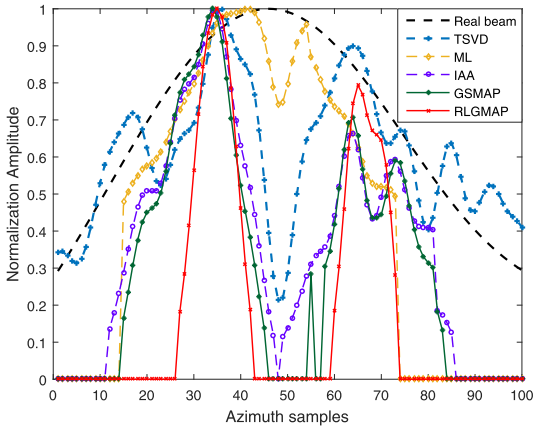

FIGURE 7. Profles of real data.

RLGMAP algorithm distinguishes the adjacent targets and has better noise suppression ability than others algorithms.

V. CONCLUSION

This paper focused on the problem of low azimuth resolution in forward-looking radar imaging of sea-surface target and proposed a deconvolution RLGMAP algorithm. The proposed RLGMAP algorithm establishes the signal model of forward-looking scanning radar as a convolution of the antenna pattern and the target scattering coefficient. Then, relying on the statistical characteristics of sea clutter and the prior knowledge of target scatters, we can obtain the iterative estimated solution based on the optimization theory to achieve azimuth superresolution. At length, the simulation and real data processing results show that the proposed algorithm not only can effectively improve the azimuth resolution and suppress sea clutter, but also can maintain stable convergence characteristics compared with other algorithms.

REFERENCES

[1] K. Morrison and J. Bennett, "Tomographic profiling—A technique for multi-incidence-angle retrieval of the vertical SAR backscattering profiles of biogeophysical targets," *IEEE Trans. Geosci. Remote Sens.*, vol. 52, no. 2, pp. 1350–1355, Feb. 2014.

[2] C. Ly, H. Dropkin, and A. Z. Manitius, "Extension of the MUSIC algorithm to millimeter-wave (MMW) real-beam radar scanning antennas," *Proc. SPIE, Radar Sensor Technol. Data Vis.*, vol. 4744, pp. 96–107, Jul. 2002.

[3] S. Uttam and N. A. Goodman, "Superresolution of coherent sources in real-beam data," *IEEE Trans. Aerosp. Electron. Syst.*, vol. 46, no. 3, pp. 1557–1566, Jul. 2010.

[4] D. Mao, Y. Zhang, Y. Zhang, Y. Huang, and J. Yang, "Doppler beam sharpening using estimated Doppler centroid based on edge detection and fitting," *IEEE Access*, vol. 7, pp. 123604–123615, 2019.

[5] Z. Chen, B. Zhang, V. Kudryavtsev, Y. He, and X. Chu, "Estimation of sea surface current from X-band marine radar images by cross-spectrum analysis," *Remote Sens.*, vol. 11, no. 9, p. 1031, May 2019.

[6] Z. Zhang, Y. Wang, and Z. Tian, "Efficient two-dimensional line spectrum estimation based on decoupled atomic norm minimization," *Signal Process.*, vol. 163, pp. 95–106, Oct. 2019.

[7] X. Zhang, L. Xu, L. Xu, and D. Xu, "Direction of departure (DOD) and direction of arrival (DOA) estimation in MIMO radar with reduced-dimension MUSIC," *IEEE Commun. Lett.*, vol. 14, no. 12, pp. 1161–1163, Dec. 2010.

[8] M. Rossi, A. M. Haimovich, and Y. C. Eldar, "Spatial compressive sensing for MIMO radar," *IEEE Trans. Signal Process.*, vol. 62, no. 2, pp. 419–430, Jan. 2014.

[9] Y. Zhang, D. Mao, Q. Zhang, Y. Zhang, Y. Huang, and J. Yang, "Airborne forward-looking radar super-resolution imaging using iterative adaptive approach," *IEEE J. Sel. Topics Appl. Earth Observ. Remote Sens.*, vol. 12, no. 7, pp. 2044–2054, Jul. 2019.

[10] W. Roberts, P. Stoica, J. Li, T. Yardibi, and F. A. Sadjadi, "Iterative adaptive approaches to MIMO radar imaging," *IEEE J. Sel. Topics Signal Process.*, vol. 4, no. 1, pp. 5–20, Feb. 2010.

[11] D. Schiavulli, F. Nunziata, M. Migliaccio, F. Frappart, G. Ramilien, and J. Darrozes, "Reconstruction of the radar image from actual DDMs collected by TechDemoSat-1 GNSS-R mission," *IEEE J. Sel. Topics Appl. Earth Observ. Remote Sens.*, vol. 9, no. 10, pp. 4700–4708, Oct. 2016.

[12] X. X. Zhu and R. Bamler, "Very high resolution spaceborne SAR tomography in urban environment," *IEEE Trans. Geosci. Remote Sens.*, vol. 48, no. 12, pp. 4296–4308, Dec. 2010.

[13] Q. Zhang, Y. Zhang, Y. Huang, Y. Zhang, W. Li, and J. Yang, "Sparse with fast MM superresolution algorithm for radar forward-looking imaging," *IEEE Access*, vol. 7, pp. 105247–105257, 2019.

[14] H. An, J. Wu, Z. Sun, and J. Yang, "A two-step nonlinear chirp scaling method for multichannel GEO spaceborne—Airborne bistatic SAR spectrum reconstructing and focusing," *IEEE Trans. Geosci. Remote Sens.*, vol. 57, no. 6, pp. 3713–3728, Jun. 2019.

[15] C. W. Chen and H. A. Zebker, "Two-dimensional phase unwrapping with use of statistical models for cost functions in nonlinear optimization," *J. Opt. Soc. Amer. A, Opt. Image Sci.*, vol. 18, no. 2, p. 338, Feb. 2001.

[16] X. Tan, W. Roberts, J. Li, and P. Stoica, "Sparse learning via iterative minimization with application to MIMO radar imaging," *IEEE Trans. Signal Process.*, vol. 59, no. 3, pp. 1088–1101, Mar. 2011.

[17] Q. Zhang, Y. Zhang, Y. Huang, and Y. Zhang, "Azimuth superresolution of forward-looking radar imaging which relies on linearized Bregman," *IEEE J. Sel. Topics Appl. Earth Observ. Remote Sens.*, vol. 12, no. 7, pp. 2032–2043, Jul. 2019.

[18] C. Liu, J. Yan, and W. Chen, "Sparse self-calibration by map method for MIMO radar imaging," in *Proc. IEEE Int. Conf. Acoust., Speech Signal Process. (ICASSP)*, Mar. 2012, pp. 2469–2472.

[19] N. Pierdicca, L. Pulvirenti, and C. Bignami, "Soil moisture estimation over vegetated terrains using multitemporal remote sensing data," *Remote Sens. Environ.*, vol. 114, no. 2, pp. 440–448, Feb. 2010.

[20] H. Xie, L. Pierce, and F. Ulaby, "SAR speckle reduction using wavelet denoising and Markov random field modeling," *IEEE Trans. Geosci. Remote Sens.*, vol. 40, no. 10, pp. 2196–2212, Jan. 2002.

[21] M. Quartulli and M. Datcu, "Stochastic geometrical modeling for built-up area understanding from a single SAR intensity image with meter resolution," *IEEE Trans. Geosci. Remote Sens.*, vol. 42, no. 9, pp. 1996–2003, Sep. 2004.

[22] A. Lopes, E. Nezry, R. Touzi, and H. Laur, "Structure detection and statistical adaptive speckle filtering in SAR images," *Int. J. Remote Sens.*, vol. 14, no. 9, pp. 1735–1758, Jun. 1993.

[23] S. Dey and T. Dey, "Bayesian estimation and prediction intervals for a Rayleigh distribution under a conjugate prior," *J. Stat. Comput. Simul.*, vol. 82, no. 11, pp. 1651–1660, Nov. 2012.

[24] A. Farina, F. Gini, M. Greco, and L. Verrazzani, "High resolution sea clutter data: Statistical analysis of recorded live data," *IEE Proc.-Radar, Sonar Navigat.*, vol. 144, no. 3, p. 121, 1997.

[25] K. Menon, N. Balakrishnan, M. Janakiraman, and K. Ramchand, "Characterization of fluctuation statistics of radar clutter for Indian terrain," *IEEE Trans. Geosci. Remote Sens.*, vol. 33, no. 2, pp. 317–324, Mar. 1995.

[26] B. A. Williams and D. G. Long, "Reconstruction from aperture-filtered samples with application to scatterometer image reconstruction," *IEEE Trans. Geosci. Remote Sens.*, vol. 49, no. 5, pp. 1663–1676, May 2011.

[27] S. Babacan, R. Molina, and A. Katsaggelos, "Bayesian compressive sensing using Laplace priors," *IEEE Trans. Image Process.*, vol. 19, no. 1, pp. 53–63, Jan. 2010.

[28] S. Chang, B. Yu, and M. Vetterli, "Adaptive wavelet thresholding for image denoising and compression," *IEEE Trans. Image Process.*, vol. 9, no. 9, pp. 1532–1546, 2000.

[29] B. C. Kelly, "Some aspects of measurement error in linear regression of astronomical data," *ApJ*, vol. 665, no. 2, pp. 1489–1506, Aug. 2007.

[30] J. N. Borge, G. R. Rodríguez, K. Hessner, and P. I. González, "Inversion of marine radar images for surface wave analysis," *J. Atmos. Ocean. Technol.*, vol. 21, no. 8, pp. 1291–1300, Aug. 2004.

[31] K. Sangston and K. Gerlach, "Coherent detection of radar targets in a non-Gaussian background," *IEEE Trans. Aerosp. Electron. Syst.*, vol. 30, no. 2, pp. 330–340, Apr. 1994.

[32] K. Evans, J. Turk, T. Wong, and G. L. Stephens, "A Bayesian approach to microwave precipitation profile retrieval," *J. Appl. Meteorol.*, vol. 34, no. 1, pp. 260–279, Jan. 1995.

[33] V. Böhm, S. Hilbert, M. Greiner, and T. A. Enßlin, "Bayesian weak lensing tomography: Reconstructing the 3D large-scale distribution of matter with a lognormal prior," *Phys. Rev.*, vol. 96, no. 12, Dec. 2017, Art. no. 123510.

[34] J. T. Macklin and N. R. Stapleton, "Radar backscatter statistics from the sea surface: Implications of SIR-C/X-SAR observations from the NE Atlantic," *J. Geophys. Res.*, vol. 103, no. C9, pp. 18827–18837, Aug. 1998.

[35] A. Gambardella and M. Migliaccio, "On the superresolution of microwave scanning radiometer measurements," *IEEE Geosci. Remote Sens. Lett.*, vol. 5, no. 4, pp. 796–800, Oct. 2008.

[36] Y. Shkvarko, "Unifying experiment design and convex regularization techniques for enhanced imaging with uncertain remote sensing data–Part I: Theory," *IEEE Trans. Geosci. Remote Sens.*, vol. 48, no. 1, pp. 82–95, Jan. 2010.

[37] T. C. Gallaudet and C. P. de Moustier, "High-frequency volume and boundary acoustic backscatter fluctuations in shallow water," *J. Acoust. Soc. Amer.*, vol. 114, no. 2, pp. 707–725, Apr. 2003.

JIANYU YANG (Member, IEEE) received the B.S. degree from the National University of Defense Technology, Changsha, China, in 1984, and the M.S. and Ph.D. degrees from the University of Electronic Science and Technology of China (UESTC), Chengdu, China, in 1987 and 1991, respectively.

He is currently a Professor with UESTC. His research interests include synthetic aperture radar and statistical signal processing. He serves as a Senior Editor for *Chinese Journal of Radio Science* and *Journal of Systems Engineering and Electronics*.

YAO KANG received the B.S. degree in electronic science and technology from Zhengzhou University, Zhengzhou, China, in 2018. She is currently pursuing the master's degree with the University of Electronic Science and Technology of China, Chengdu, China. Her research interests include signal processing and radar imaging.

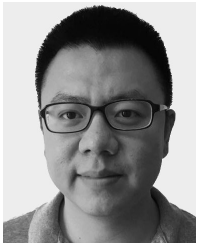

YIN ZHANG (Member, IEEE) received the B.S. and Ph.D. degrees in electronic information engineering from the University of Electronic Science and Technology of China (UESTC), Chengdu, China, in 2008 and 2016, respectively.

From 2015 to 2016, he was a Visiting Student with the University of Delaware, Newark, DE, USA. He is currently an Associate Research Fellow with the School of Information and Communication Engineering, UESTC. His research interests include radar imaging and signal processing in related radar applications.

YULIN HUANG (Senior Member, IEEE) received the B.S. and Ph.D. degrees from the School of Electronic Engineering, University of Electronic Science and Technology of China (UESTC), Chengdu, China, in 2002 and 2008, respectively.

From 2013 to 2014, he was a Visiting Researcher with the University of Houston, Houston, TX, USA. He is currently a Professor with the School of Information and Communication Engineering, UESTC. His research interests include synthetic aperture radar, target detection and recognition, artificial intelligence, and machine learning.

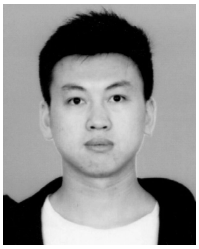

YONGCHAO ZHANG (Member, IEEE) received the B.S. degree in electronic information engineering from Hainan University, Haikou, China, in 2011, and the Ph.D. degree from the School of Information and Communication Engineering, University of Electronic Science and Technology of China (UESTC), Chengdu, China, in 2018.

From 2016 to 2017, he was a Visiting Student with Lund University, Lund, Sweden. He is currently an Associate Research Fellow with the School of Information and Communication Engineering, UESTC. His research interests include array signal processing and inverse problem in radar applications.